JACS
JOURNAL OF THE AMERICAN CHEMICAL SOCIETY

ARTICLE

pubs.acs.org/JACS

Gating the Mechanistic Pathway to the Elusive 4-Membered Ring Azeteoporphyrin

David F. Dye, Tillmann Köpke, Raghunath O. Ramabhadran, Krishnan Raghavachari,* and Jeffrey M. Zaleski*

Department of Chemistry, Indiana University, Bloomington, Indiana 47405, United States

Supporting Information

ABSTRACT: Photolysis of metalated (Cu and Ni) and free base 2-diazo-3-oxochlorins within a frozen matrix (λ = 457.9 nm, toluene, 80 K) generates a single photointermediate with a hypsochromically shifted electronic absorption spectrum relative to the starting diazochlorins. The appearance of ketene (~2131 cm^{-1}) and azete (~1670 cm^{-1}) vibrations in infrared absorption and Raman spectra, respectively, identifies this intermediate as resulting from the Wolff rearrangement of the diazochlorins upon N_2 loss. Computational modeling of the vibrational spectra and TDDFT simulation of the electronic transitions of potential photointermediates corroborate this assignment. Isolation and analysis of photoproducts of these diazochlorins formed within *n*-butanol-doped frozen toluene matrices indicate near exclusive formation of azeteoporphyrins. In sharp contrast, room temperature laser photolysis of these materials yields a mixture of photoproducts deriving from the presence of both carbene and ketene intermediates. Computational modeling of the intramolecular reactivity of the proposed sp^2 carbene intermediate shows exclusive bond insertion to the adjacent phenyl group, and no evidence of Wolff rearrangement. Computational reaction profile analyses reveal that the barrierless Wolff rearrangement proceeds via an out-of-plane carbene electronic configuration that is generated directly during the loss of N_2. The formation of out-of-plane carbene, resulting in the exclusive formation of the observed ketene photointermediate at low temperatures, is consistent with orbital symmetry considerations and by the geometric constraints imposed by the frozen matrix. Combined, this leads to a model showing that azeteoporphyrin formation via the Wolff rearrangement is dependent upon the structural disposition of the adjacent framework, and the specific reaction intermediate formed is very sensitive to this feature.

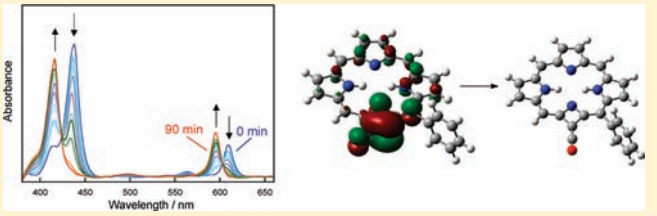

INTRODUCTION

Photochemical porphyrin reactions have a diverse and distinguished history rich in utility within the themes of photodynamic therapy and $^1O_2$ generation,[1−8] optoelectronic devices,[9−17] photovoltaic materials,[18−27] and photoinduced energy or charge transport in dye-sensitized solar energy cells.[28−37] All of the key excited- or ground-state chemical properties that make these applications plausible derive from the fundamental electronic character of the basic porphyrin skeleton, modulated by peripheral substitution, or the reactivity of those substituents. Within this paradigm, we continue to pursue the development of tetrapyrrole frameworks containing radical-generating peripheral functionality that have potential as probes or O_2-independent PDT agents for biology/medicine. Constructs supporting pyrrole-based 1,2-diyne[38−45] or diazo-ketyl[46−50] functionalities have been shown in some cases, to photochemically generate cyclized phenyl diradicals via Bergman cyclization,[41] or carbene intermediates instantaneously upon photochemical loss of N_2 (Figure 1).[49,50] In addition to reacting with external quenchers or nucleophilic reagents, these *meso*-tetraphenyl-based frameworks are predisposed to internal radical trapping, which gives rise to highly unique, extended π-system porphyrinoid structures that possess modulated electronic properties. In the case of diazo-ketyl substitution, another unusual reaction pathway is clearly observed: pyrrole ring contraction via the Wolff rearrangement[51] to yield the unprecedented 4-membered ring-containing azeteoporphyrin.[49,50] Such an extraordinary product and transformation could only derive from a ketene intermediate formed concertedly or sequentially via an instantaneous carbene.

These observations are only contextual within the framework of traditional diazo-ketone photoreactivity and mechanism that has been so impressively detailed via low temperature trapping studies, ultrafast spectroscopic measurements, and detailed potential energy surface reaction trajectories. Chapman and coworkers originally demonstrated the photoconversion of a carbene trapped upon loss of N_2 from a cyclic α-diazoketone to a stable ketene intermediate at low temperature.[52] Recently, Platz et al. have used ultrafast transient spectroscopic methods to determine that similar carbene-to-ketene conversions can also occur in fluid solution, on the pico- and subpicoseond time scales,[53,54] thereby providing continuity and support for Chapman's earlier observations at low temperature. Further ultrafast spectroscopic measurements have confirmed the conversion of a

Received: April 26, 2011
Published: June 30, 2011

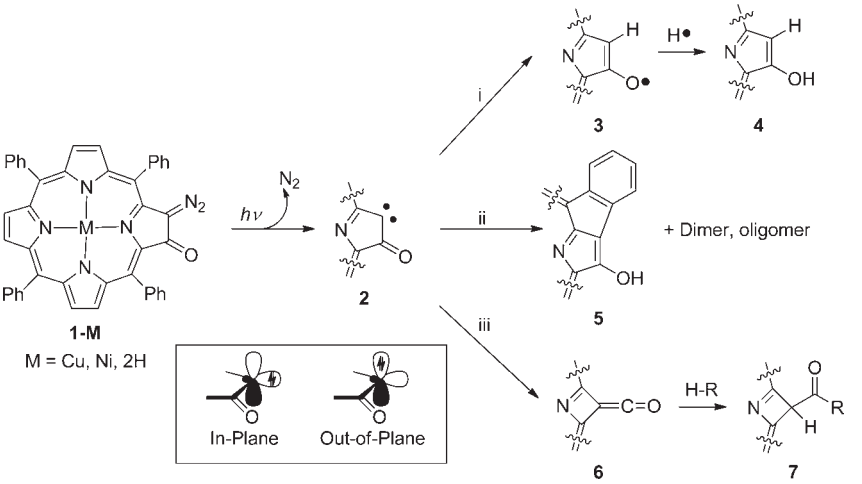

Figure 1. Photochemical N_2 release from diazochlorins and subsequent carbene reaction pathways. Hydrogen abstraction (i) and internal C−H bond insertion (ii) are proposed to proceed through an "in-plane" carbene intermediate, while Wolff rearrangement products (iii) are considered to require an "out-of-plane" electronic arrangement.

vibrationally hot carbene to a ketene intermediate,[55] as well as concerted Wolff rearrangements that directly form ketene intermediates and bypass the initial carbene species.[56,57] Indeed, many α-diazoketones demonstrate products consistent with both concerted and stepwise Wolff rearrangement mechanisms,[58] suggesting both pathways could contribute to observed photoproduct distributions. Additionally, potential energy surface reaction trajectory calculations for a subset of cyclic and acyclic α-diazoketones indicate that the preference for the Wolff rearrangement and ketene formation versus stable carbene intermediate is heavily dependent on the orthogonality of the diazoketone dihedral angle, which permits stabilization of the carbene by conjugation with the carbonyl π-system at angles upward of 60°.[59]

From this elegant work, a consistent picture emerges regarding the mechanistic pathways of diazo-ketone photoreactivity. Photochemical preparation of singlet carbene intermediates on the femtosecond time scale results in a planar ketocarbene conformation that relaxes to an orthogonal structure to facilitate overlap of the carbene orbital with the π-system of the carbonyl. For acyclic systems, such a rearrangement is generally accessible with little thermodynamic penalty. However, for cyclic carbene frameworks, complete orthogonal reorientation is hindered by ring strain, the singlet carbene is not stabilized, and a kinetically concerted intramolecular Wolff rearrangement and ring contraction with subsequent ketene formation becomes the dominant reaction pathway for the diradical.

Although such reactivity trends appear clearly defined, molecular architecture can play a significant role in perturbing these delicate reaction trajectories. Our observations that visible photoirradiation of 1,2-diazo-oxochlorins produces a mixture products deriving from both radical addition reactivity, as well as Wolff ring contraction of the macrocycle to form unprecedented azeteoporphyrins,[49,50] clearly exemplifies the need to understand these reaction trajectories within the context of carbene/ketene photochemical tradition and manipulate them to maximize desired product formation. The porphyrinoid backbone structures upon which these architectures are based afford a convenient spectroscopic handle for investigation of the mechanistic pathways responsible for the convolved photoproduct formation. To this end, we describe low temperature electronic and vibrational spectroscopic analysis of the initial steps in the photoconversion of free base, Cu(II), and Ni(II) 1,2-diazooxochlorins to identify the primary intermediates formed upon N_2

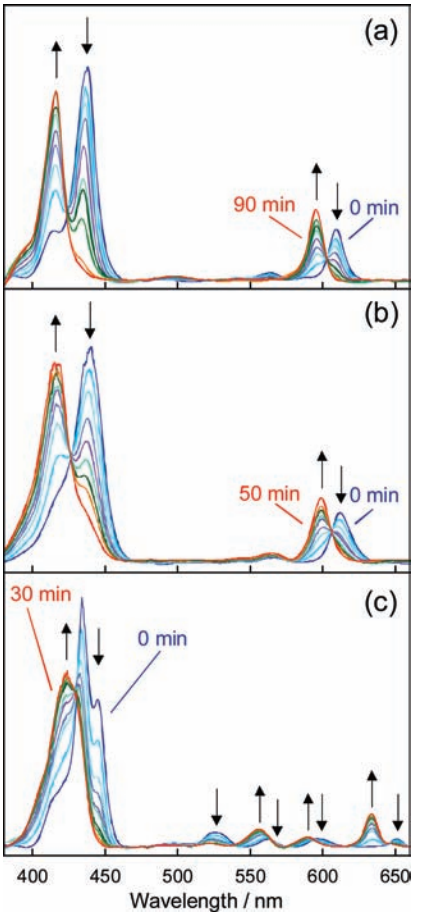

Figure 2. Electronic absorption spectra of **1-Cu** (a), **1-Ni** (b), and **1-2H** (c) exhibit similar bathochromic shifts in both Soret and Q bands upon photolysis (λ_{exc} = 457.9 nm) of frozen toluene solutions at 2 K (**1-Cu** and **1-Ni**) and 80 K (**1-H2**).

dx.doi.org/10.1021/ja203451k |J. Am. Chem. Soc. 2011, 133, 13110–13120

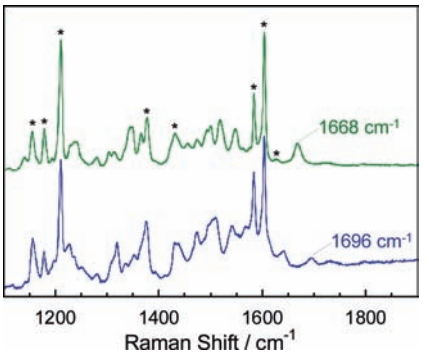

Figure 3. Resonance Raman spectra of **1-Cu** (top, green) and **1-Ni** (bottom, blue) in frozen toluene matrices (77 K) show evidence of an azete C_m-C_α vibration after 60 and 240 min of photolysis, respectively (λ_{exc} = 457.9 nm, 110 mW). Solvent peaks are marked with asterisks (*).

loss and their evolution to photoproducts. Computational analyses of the reaction pathways, in conjunction with spectroscopic assignments, lend critical insight into the structural conditions that control specific intermediate and product formation.

RESULTS AND DISCUSSION

Electronic Absorption Spectroscopy. The electronic absorption spectra of **1-Cu** and **1-Ni** in toluene glasses at 2 K both exhibit an intense Soret band ($\lambda_{\mathbf{1\text{-}Cu}}$ = 438 nm, $\lambda_{\mathbf{1\text{-}Ni}}$ = 440 nm), a lower energy Q-band ($\lambda_{\mathbf{1\text{-}Cu}}$ = 609 nm, $\lambda_{\mathbf{1\text{-}Ni}}$ = 612 nm), and a vibrationally excited, lower intensity Q-band ($\lambda_{\mathbf{1\text{-}Cu}}$ = 563 nm, $\lambda_{\mathbf{1\text{-}Ni}}$ = 565 nm). Upon photolysis of **1-Cu** (t = 90 min) and **1-Ni** (t = 50 min) with λ_{exe} = 457.9 nm (110 mW), these features are bleached, and the isosbestic appearance of new, hypsochromically shifted spectra is observed for both the copper (λ_B = 416, λ_Q = 595 nm, Figure 2a) and the nickel (λ_B = 415, λ_Q = 599 nm, Figure 2b) diazo-oxochlorins, indicating the formation of a single, similar photointermediate for both. The vibrationally excited Q-bands of the intermediate were not clearly discernible, although the relatively low extinction coefficients observed for these features in the starting diazochlorin absorption spectrum make this observation unsurprising.

Warming of the intermediate produced from the photolysis of **1-Cu** to 90 K produced no pronounced changes in its electronic absorption spectrum beyond minor heating-induced broadening and red shifts (Δ < 3 nm, Figure S1). Photolysis of a second **1-Cu** sample at 80 K (90 min, λ_{exe} = 457.9 nm, 110 mW) generated an intermediate with spectral features identical to those observed for the first sample at comparable temperatures, confirming that liquid nitrogen cooling is sufficient to trap the species initially observed at 2 K.

The electronic absorption of **1-2H** (80 K, toluene glass) exhibits a split Soret band (λ_B = 434 and 445 nm) and four Q-bands (λ_Q = 526, 561, 595, and 651 nm) arising from the descent in symmetry from pseudo-D_{4h} to pseudo-D_{2h} upon demetalation and protonation of the pyrrole nitrogens to generate unique x and y molecular axes. These features hypsochromically shift (λ_B = 423 nm with a 430 nm shoulder; λ_Q = 522, 556, 590, and 634 nm) upon photolysis (λ_{exe} = 457.9 nm, 110 mW, 30 min) (Figure 2c), and although there is a degree of overlap between the two high-energy Q-bands before and after photolysis, the clear isosbestic points apparent in the conversion of both the Soret and the Q-bands, coupled with the complete

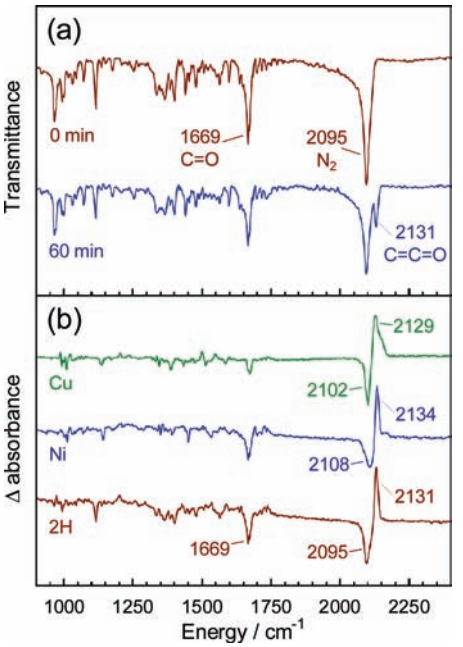

Figure 4. (a) Infrared absorption spectra of **1-2H** at 93 K before and after photolysis (λ_{exc} = 457.9 nm, 100 mW, 60 min) shows the appearance of a ketene stretch at 2131 cm^{-1} and a corresponding decrease in intensity of ketone (1669 cm^{-1}) and diazo (2095 cm^{-1}) stretches. (b) Differences of absorption spectra recorded before and after photolysis of **1-Ni** and **1-Cu** under the same conditions show similar diagnostic features.

bleaching of the 445 nm peak of **1-2H**, indicate the uniform conversion to a single photointermediate.

The similar red-shifts of the electronic spectra of each of the diazo-chlorins upon photolysis at low temperatures indicate a preserved reaction pathway to intermediates with decreased aromatic delocalization for each of the diazochlorins. The presence of a ring-contracted azete in the ketene (**6-M**) and an unoccupied p_z orbital in the carbene (**2-M**) would be expected to disrupt the macrocycle π system, and a qualitative analysis of either could suggest blue-shifted spectral features. Conversely, an intramolecular phenyl insertion would be expected to increase π delocalization and red-shifted spectral features would be expected, as is consistent with TD-DFT calculations of the electronic absorption spectra of these photointermediates (*vide infra*). Thus, the electronic absorption spectra are most consistent with the conversion of diazochlorins to ketenes upon photolysis in a frozen matrix.

Vibrational Spectroscopy. Resonance Raman and infrared absorption (IR) spectroscopies were used to confirm the assignment of the trapped photointermediate as a ketene by correlation of spectroscopically observed molecular vibrations to those expected for a ketene. The most diagnostic vibrational spectroscopic feature reported for ketene intermediates trapped during Wolff rearrangements is the strongly IR allowed C═C═O ketene stretch.[51,52,56]

Resonance Raman spectra (λ_{exc} = 457.9 nm, 110 mW, 60 min integration) of frozen toluene solutions of **1-Cu** and **1-Ni** (Figure 3) were recorded after and 60 and 240 min of photolysis, respectively. Attempts to record Raman spectra of the photointermediate of **1-2H** were hindered by strong visible fluorescence obscuring the Raman signal. The observed vibrations

Table 1. Thin Layer Chromatographic Retention Factors (Silica Gel, 1:1 DCM:MeOH Eluent), Mass, and Soret Peak Positions of Photoproducts Generated from Frozen Matrix (77 K) and Room Temperature (rt) Photolyses of 1-M in 4:1 Toluene:BuOH[a]

	R_f	color	m/z	Soret/nm	assignment
1-2H 77 K	0.46	blue	703.2	412	**7-2H**
	0.33	maroon	657.2	424	**1-2H**
1-Ni 77 K	0.69	blue	758.1	403	**7-Ni**
	0.53	green	713.0	431	**1-Ni**
1-Cu 77 K	0.70	blue	764.2	410	**7-Cu**
	0.54	green	718.1	431	**1-Cu**
1-Ni rt	0.73*	blue*	758.0		**7-Ni**
	0.64	green	846.1	413	OBu and Bz radical addition
	0.58	red	685.0	409	**4-Ni**
	0.52*	green*	713.0		**1-Ni**
	0.43	green	684.1	429	**5-Ni**

[a] Minor products are marked with asterisks (*).

between 1150 and 1600 cm^{-1} have been assigned to various in-plane macrocycle stretches by comparison with calculated normal modes (*vide infra*). Many of these features are convolved with toluene vibrations, complicating observation of these peaks. The vibrations observed at 1668 cm^{-1} for **1-Cu** and 1696 cm^{-1} for **1-Ni** fortunately fall well away from any toluene vibrations, and have been assigned as an azete C_m-C_α stretch, indicating the presence of a ring-contracted ketene intermediate. Raman spectra were recorded at 2200 cm^{-1} (not shown) in an attempt to directly observe a definitive ketene C═C═O stretch, but no diagnostic signals were observed in this region. This is consistent with computational results (*vide infra*) indicating that this stretch is not strongly Raman-allowed. These calculations also indicate that the infrared absorption of a ketene stretch should be very intense. Thus, spectra of **1-2H**, **1-Cu**, and **1-Ni** were recorded at 93 K as ground microcrystalline powders in pressed KBr pellets. Each sample was photolyzed (λ_{exc} = 457.9 nm, 100 mW, 60 min), and although the photolysis times and conditions for these samples were on the same order as those for the low-temperature electronic absorption experiment that showed complete conversion to photoproduct, the high optical density of the microcrystalline samples prevented complete photolysis (Figure 4a).

Differences in IR absorption spectra recorded before and after photolysis clearly show bleaching of the diazo N═N (**1-Cu**, 2102 cm^{-1}; **1-Ni**, 2108 cm^{-1}; **1-2H**, 2090 cm^{-1}) and carbonyl C═O (1669 cm^{-1} for all three) vibrations, accompanied by the appearance of a new ketene C═C═O stretch (**1-Cu**, 2129 cm^{-1}; **1-Ni**, 2134 cm^{-1}; **1-2H**, 2131 cm^{-1}) (Figure 4b), directly confirming the identity of the trapped photointermediate as a ketene.

Frozen Matrix Photolysis. Frozen solutions of **1-Ni**, **1-Cu**, and **1-2H** in 4:1 toluene:*n*-butanol mixtures were photolyzed (λ_{exe} = 457.9 nm, 110 mW) at 77 K for 30 min, thawed, and the resulting photoproducts were separated by thin layer chromatography (TLC). Each of these photolysis experiments produced similar results with two predominant products observed for each experiment: a primary product consistent in both color and R_f for the associated Wolff rearrangement products **7-2H** (blue, R_f = 0.46), **7-Ni** (blue, R_f = 0.69), and **7-Cu** (blue, R_f = 0.70), and a product corresponding to unreacted **1-2H** (maroon, R_f = 0.33),

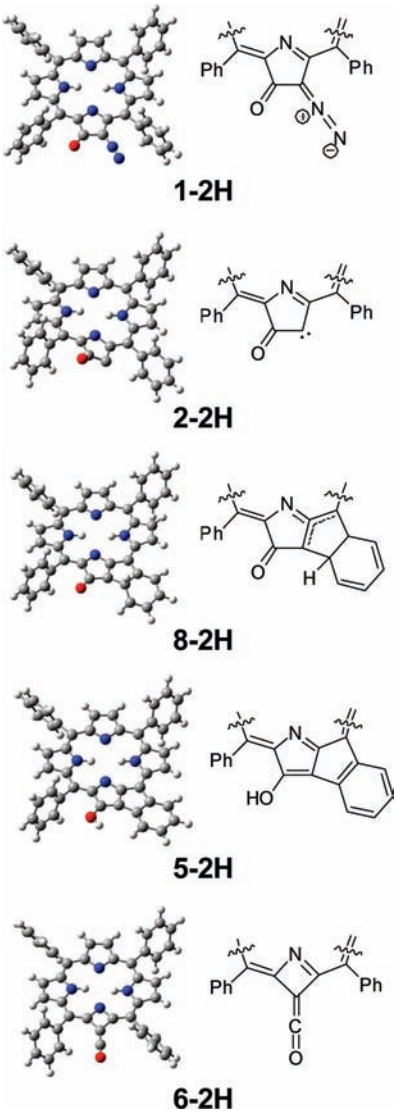

Figure 5. Calculated structures (B3LYP/6-31 g(d,p)) of **1-2H**, photointermediates, and photoproducts used for simulation of spectroscopic features.

1-Ni (green, R_f = 0.53), and **1-Cu** (green, R_f = 0.54) (Table 1). Each of the products was extracted from the TLC plate and analyzed by mass spectroscopy and electronic absorption spectroscopy, with both the mass and the Soret peak positions confirming product assignments. The presence of unreacted **1-M** in each of the mixtures is attributed to incomplete photoconversion of the center of the frozen samples due to their large optical densities. No residual material at R_f = 0 was observed for any of the low-temperature photolysis reactions. An additional emerald green azeteoporphyrin photoproduct with an R_f slightly smaller than the parent diazochlorins was also observed in low yields (>10%) for the photolysis of **1-Cu** and **1-Ni**.

The predominance of the Wolff rearrangement products in each of the photolyzed samples convincingly confirms the trapping of ketenes in the frozen matrices, which undergo nucleophilic addition of *n*-butanol upon thawing and warming. Additionally, the lack of any observed material with $R_f \approx 0$ indicates the absence of any high molecular weight products typically formed via radical−radical coupling when diazochlorins

dx.doi.org/10.1021/ja203451k |*J. Am. Chem. Soc.* 2011, 133, 13110–13120

Table 2. Comparison of Select Observed (IR) and Computed Vibrations of 1-2H

assignment	observed/cm^{-1}	calculated/cm^{-1}	difference/cm^{-1}	deviation (%)
C_β═N═N stretch	2095	2162	67	3.20
C_β═O stretch	1670	1723	53	3.17
phenyl sym stretch	1598	1607	9	0.56
C_α−C_m stretch	1563	1549	−14	−0.90
pyrrole breathing	1479	1484	5	0.34
C_α−C_m asym stretch	1455	1448	−7	−0.48
phenyl asym stretch	1441	1438	−3	−0.21
C_β═N_2 stretch	1400	1406	6	0.43
C_α−C_β−N_p stretch	1385	1378	−7	−0.51
asym C_α−C_β−N_p stretch	1367	1365	−2	−0.15
sym C_α−C_β−N_p stretch	1337	1334	−3	−0.22
$C_{\beta O}$−$C_{\beta N2}$ Stretch	1116	1103	−13	−1.16
C−H in plane wag	1073	1072	−1	−0.09
sym C_α−C_β−N_p stretch (protonated pyrroles)	995	989	−6	−0.60
sym C_α−C_β−N_p stretch (opposite diazo-oxo pyrrole)	966	961	−5	−0.52
C_β−H out-of-plane wag	799	793	−6	−0.75
C_{ph}−H out-of plane wag	752	746	−6	−0.80
N_p−H out-of-plane wag	720	720	0	0.00

have been photolyzed at room temperature.[48−50] This absence strongly suggests that carbene species are not present in solution when molecules are able to diffuse and react bimolecularly.

To confirm that monochromatic laser photolysis produced photoproduct distributions similar to those observed under broad-band irradiation,[50] a portion of the **1-Ni** solution prepared for low-temperature photolysis was irradiated (λ_{exe} = 457.9 nm, 110 mW, 30 min) at room temperature. Separation via TLC indicated the presence of four distinct photoproducts and a large amount of residual material at R_f = 0. The minor product (<10%) was consistent in R_f, color, and mass with the Wolff photoproduct, **7-Ni** (0.73, blue, 758.0 m/z). The three major products were observed as an intense red spot corresponding to the "hydroxy" photoproduct **4-Ni** (R_f = 0.58, 658 m/z, λ_B = 409 nm) and two intense green spots corresponding to the "phenyl-quenched" photoproduct **5-Ni** (R_f = 0.43, 648.1 m/z, λ_B = 429 nm) and a previously uncharacterized photoproduct (R_f = 0.64, 846.1 m/z, λ_B = 413 nm).[49,50] This new material is tentatively assigned as the radical addition product of both a butoxy and a benzyl group to **2-Ni** on the basis of mass spectrometry. Residual material at R_f = 0 is consistent with mixtures of high molecular weight, polymeric, radical addition products generated during benchtop photolysis that similarly resist elution from silica gel. The diversity of photoproducts isolated from monochromatic benchtop photolysis clearly demonstrates that cooling is necessary for exclusive ketene formation.

Geometry Optimizations and Vibrational Energy Calculations. Gas-phase optimized geometries and molecular vibrations of **1-2H**, associated reaction intermediates, and photoproducts were calculated using density functional theory (DFT) at the B3LYP/6-31G(d,p) level of theory (Figure 5). Comparison of the calculated vibrational frequencies of **1-2H** shows excellent agreement with those observed via infrared absorption spectroscopy (Table 2) after applying a uniform scale factor of 0.9735. Most calculated in-plane macrocycle normal modes are within 1% of the experimentally observed values, although the C_β═N═N and C_β═O stretches show ∼3% deviation.

The scaling factor was purposely iterated to best model the macrocycle vibrations, while leaving the largest deviation in the most straightforwardly detected C_β═N═N and C_β═O stretches. The latter two vibrations of the peripheral moieties are different from the macrocycle modes insofar as they are not directly coupled to the core aromatic structure, and hence are expected to be more heavily influenced by their environment. Thus, the larger discrepancy between the calculated and observed C_β═N═N and C_β═O stretches is not unexpected, although this deviation is still within the error expected for this level of theory.[60] Furthermore, both of the IR absorptions for these vibrations are intense and occur outside the region of other strong vibrations, allowing definitive assignment of these normal modes despite a higher deviation between calculated and observed frequencies.

Calculated normal modes of **2-2H** and **6-2H** show perturbations in the core macrocycle modes, but the most diagnostic vibrational features of these photointermediates are those associated with the carbonyl and azete moieties. As has been discussed, the calculated diazo and carbonyl stretches of **1-2H** occur at 2162 and 1713 cm^{-1} (Figure 6a and b) and agree well with the observed values of 2095 and 1670 cm^{-1}, respectively. Upon loss of N_2 to generate **2-2H**, the carbene carbonyl stretch (Figure 6c, 1713 cm^{-1}) is predicted to shift to slightly lower frequency relative to the **1-2H** carbene stretch, accompanied by the obvious absence of a diazo vibration. The internal ring contracted photointermediate **6-2H** is predicted to exhibit two new, distinct diagnostic normal modes not present the tetrapyrrole structures, an azete C_m−C_α stretch at 1645 cm^{-1} (Figure 6d) and a ketene stretch at 2163 cm^{-1} (Figure 6e).

Comparison of these calculated values with the low-temperature IR absorption spectrum of photolyzed **1-2H** shows good agreement of the predicted ketene stretching frequency with the newly appearing 2131 cm^{-1} vibration observed after photolysis (−31 cm^{-1} difference, 1.5% deviation). The azete vibration is clearly observed in the Raman spectra of photolyzed **1-Cu** and **1-Ni** at 1668 and 1696 cm^{-1}, respectively, which are quite close to the observed 1669 cm^{-1} carbonyl stretch observed via IR

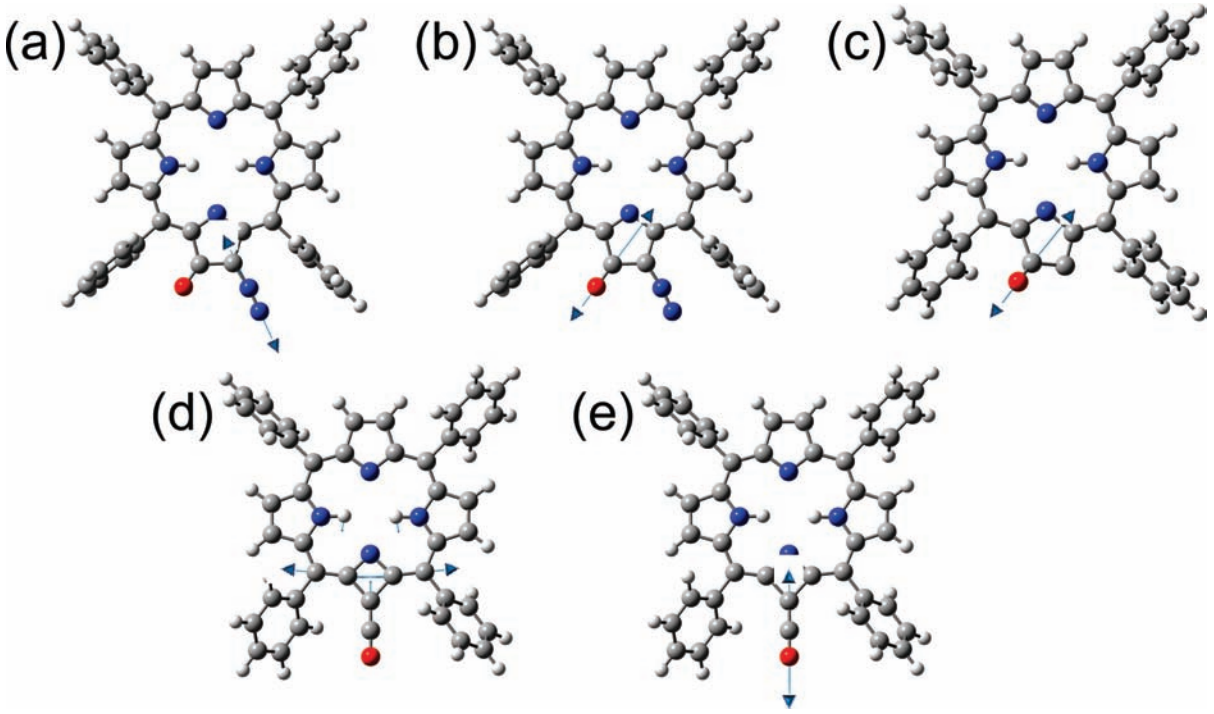

Figure 6. Calculated molecular vibration for **1-2H**, **2-2H**, and **6-2H**: (a) diazo stretch (2169 cm^{-1}), (b) ketone stretch (1729 cm^{-1}), (c) ketocarbene stretch (1713 cm^{-1}), (d) azete C_m-C_α stretch (1645 cm^{-1}), and (e) ketene stretch (2163 cm^{-1}).

absorption for both of these starting diazochlorins. Indeed, the difference IR spectrum of **1-Cu** and its photointermediate does not show a distinct new azete peak due to the overlap of the carbonyl vibration, although the difference spectra of **1-Ni** and **1-2H** do exhibit new features at ~1690 cm^{-1} that are not clearly resolved. These compare very favorably with the IR spectra of the butanol Wolff addition products, which show a prominent ketone signature at ~1735 cm^{-1} (**1-2H**, 1734 cm^{-1}; **1-Ni**, 1737 cm^{-1}; **1-Cu**, 1734 cm^{-1}) and a weak vibrational feature at ~1660 cm^{-1} (**1-2H**, 1653 cm^{-1}; **1-Ni**, 1675 cm^{-1}; **1-Cu**, 1653 cm^{-1}).[50]

The intensity of the observed azete C_m-C_α stretch is predicted to be larger as compared to other macrocycle vibrations for Raman spectroscopy versus IR absorption spectroscopy. This is consistent with the observation that the azete vibration is more clearly defined in the Raman spectra of the trapped photointermediates than in the corresponding IR spectra. Conversely, the ketene stretch is predicted to be the most predominant feature in its IR absorption spectrum (approximately 5 times larger than the second most intense vibration), while Raman scattering activity associated with this stretch is predicted to be very weak (approximately 400 times less intense than the largest Raman peak). These calculated intensities corroborate the appearance of ketene vibration in the IR spectrum and the absence of the equivalent features in the Raman spectra of these complexes.

Electronic Transitions via Time-Dependent Density Functional Theory (TDDFT). The first 15 singlet excited states of **1-2H**, **5-2H**, **6-2H**, and **8-2H**, and the first 30 singlet excited states of **2-2H** were calculated using TDDFT to elucidate electronic transitions for isolated materials and to predict electronic absorption spectra of uncharacterized reaction intermediates. These results are summarized in Table 3.

Four vertical electronic excitations are apparent for **1-2H** in the visible spectrum arising from transitions between the four frontier orbitals (LUMO+1, LUMO, HOMO, HOMO−1) that closely resemble those which Gouterman identified as being responsible for the predominant visible transitions of porphyrins.[61,62] Some mixing of the peripheral oxygen and diazo π systems into the Gouterman orbitals is apparent (Figure S2a), although this does not result in significant deviation of the electronic transitions from those expected of a nonfunctionalized porphyrin. The two low-energy transitions at 582 and 554 nm are assigned as the Q-bands, and although four Q-bands are spectroscopically observed due to vibronic coupling to the electronic transition, this coupling was not modeled, and thus only two Q-band excitation energies have been calculated. Of note are the relatively low predicted oscillator intensities of the calculated Q-bands, although this is consistent with other TDDFT studies of porphyrin electronic excitations.[63−65] The two higher energy electronic excitations at 438 and 432 nm are primarily comprised of transitions to the LUMO+1 orbital and are assigned to the Soret or B-band.

Transitions from the carbene lone pair to the associated unoccupied p_z orbital that form the HOMO and LUMO, respectively, of **2-2H** (Figure S2b) contribute significantly to an electronic absorption spectrum that varies greatly from that of a typical porphyrinoid. Although Gouterman orbitals are present in the calculated electronic structure of **2-2H**, the unoccupied p_z LUMO is 1.52 eV lower in energy than the low-energy Gouterman π^* (LUMO+1), providing an alternative to electronic excitations that would populate a Gouterman LUMO in typical porphyrins. Thus, several long-wavelength transitions that are less intense and lower in energy than those expected of typical porphyrin $\pi \rightarrow \pi^*$ absorptions are observed at 1101, 740, and 523 nm. Excitations from the phenyl π orbitals to the LUMO ($\pi_{ph} \rightarrow p_z$) at 487, 449, 442, and 441 nm similarly have calculated intensities lower than expected for Gouterman transitions.

Table 3. Calculated (TD-B3LYP/6-31+g(d,p)) Vertical Electronic Absorption Energies, Oscillator Strengths (f), and Two Primary Electronic Transitions for 1-2H, 2-2H, 5-2H, 6-2H, and 8-2H in Dichloromethane (SMD)[a]

	absorption	f	electronic transitions		assignment
1-2H					
1	582 nm (2.13 eV)	0.015	HOMO−1 → LUMO (59%)	HOMO → LUMO+1 (37%)	Q1
2	554 nm (2.24 eV)	0.060	HOMO−1 → LUMO+1 (28%)	HOMO → LUMO (67%)	Q2
3	438 nm (2.83 eV)	0.890	HOMO−1 → LUMO+1 (33%)	HOMO → LUMO+1 (23%)	B
4	423 nm (2.93 eV)	1.462	HOMO−1 → LUMO+1 (28%)	HOMO → LUMO (30%)	B
2-2H					
1	1101 nm (1.13 eV)	0.046	HOMO−1 → LUMO (28%)	HOMO → LUMO (66%)	n → p_z
2	740 nm (1 68 eV)	0.087	HOMO−2 → LUMO (61%)	HOMO−1 → LUMO (26%)	π_g → p_z
4	523 nm (2.37 eV)	0.044	HOMO−5 → LUMO (30%)	HOMO−4 → LUMO (24%)	π → p_z
5	521 nm (2 38 eV)	0.145	HOMO−1 → LUMO+2 (25%)	HOMO → LUMO+1 (36%)	Q1
7	487 nm (2 55 eV)	0.019	HOMO−12 → LUMO (42%)	HOMO−7 → LUMO (14%)	π_{ph} → p_z
8	463 nm (2.68 eV)	0.068	HOMO−8 → LUMO (42%)	HOMO−2LUMO +1(14%)	Q2
9	461 nm (2.69 eV)	0.182	HOMO−7 → LUMO (40%)	HOMO−2 → LUMO+1 (18%)	Q2
11	449 nm (2.76 eV)	0.086	HOMO−12 → LUMO (28%)	HOMO−9 → LUMO (25%)	π_{ph} → p_z
12	442 nm (2.80 eV)	0.023	HOMO−10 → LUMO (68%)	HOMO−9 −+LUMO (15%)	π_{ph} → p_z
13	441 nm (2 81 eV)	0.087	HOMO−11 → LUMO (59%)	HOMO−9 → LUMO (16%)	π_{ph} → p_z
14	438 nm (2 83 eV)	0.421	HOMO−2 → LUMO+2 (18%)	HOMO−1 → LUMO+2 (35%)	B
15	403 nm (3.O8 eV)	0.115	HOMO−13 → LUMO (78%)	HOMO−2 → LUMO+1 (11%)	B
16	396 nm (3.13 eV)	0.432	HOMO−14 → LUMO (54%)	HOMO−2 → LUMO+1 (22%)	B
17	392 nm (3.16 eV)	0.371	HOMO−14 → LUMO+2 (63%)	HOMO−2 → LUMO+2(19%)	B
19	379 nm (3 27 eV)	0.526	HOMO−2 → LUMO+2 (63%)	HOMO−1 → LUMO+2 (9%)	B
5-2H					
1	667 nm (1 0.86 eV)	0.095	HOMO → LUMO (79%)	HOMO → LUMO+1 (11%)	Q1
2	611 nm (2.03 eV)	0.036	HOMO−1 → LUMO (37%)	HOMO → LUMO+1 (53%)	Q2
3	480 nm (2.58 eV)	0.348	HOMO−2 → LUMO+1 (30%)	HOMO−1 → LUMO (35%)	B
4	425 nm (2.92 eV)	1.582	HOMO−2 → LUMO (11%)	HOMO−1 → LUMO+1 (50%)	B

[a] Oscillators with energies greater than 3.10 eV (3.30 eV for **2-2H**) or intensities less than 0.015 have been omitted.

The large 2.34 eV gap between the highest occupied and lowest unoccupied Gouterman orbitals (HOMO−1 and LUMO+1) results in significantly higher Q and Soret band energies than calculated for **1-2H**. The **2-2H** 521 nm transition has been assigned as the low energy Q-band (Q1) due to the strong contribution of the HOMO−1 → LUMO+2 transition between Gouterman orbitals (25%) and its relatively large oscillator strength (0.145) as compared to others in this spectral region. The primary contribution to this excitation, HOMO → LUMO+1 (36%), would rigidly be assigned as n → π^*, although there is a degree of mixing between the carbene sp^2 orbital and the porphyrin π system arising from the geometric overlap between these orbitals (induced by the out-of-plane deformation of the carbene carbon upon loss of N_2), giving this transition a degree of $\pi \rightarrow \pi^*$ character (Figure S2d). The excitations at 463 and 461 nm both have contributions from an HOMO−2 → LUMO+1 transition between Gouterman orbitals, resulting in the assignment of both of these transitions as contributing to the higher-energy Q2 band. Although the primary contributor for each transition is $\pi_{ph} \rightarrow p_z$ in nature, their large oscillator strengths (0.068 and 0.145 respectively) relative to the other $\pi_{ph} \rightarrow p_z$ excitations again suggest that the Gouterman transition significantly contributes to the character of these excitations. Only the two intense absorptions at 438 and 379 nm have primary contribution from transitions between Gouterman orbitals (HOMO−2 → LUMO+2 and HOMO−1 → LUMO+2). These absorptions, along with the absorptions at 403, 396, and 392 nm that have secondary contributions from HOMO−2 → LUMO+1 transitions between Gouterman orbitals, contribute to a split Soret band. The resulting spectrum of the carbene is thus predicted to be quite different from that observed for the trapped photoproduct.

In sharp contrast, the ketene photointermediate **6-2H** is predicted to exhibit a typical porphyrinic visible spectrum dominated by electronic transitions between Gouterman orbitals. Two Q-bands are predicted at 568 and 553 nm, and two absorptions contributing to the Soret band are predicted at 415 and 400 nm. All four of these transitions occur between the Gouterman-like LUMO+1, LUMO, HOMO, and HOMO−1 orbitals (Figure S2d), although the splitting between the LUMO and LUMO+1 is relatively large (0.48 eV) due to the marked difference between the x and y molecular axes induced by pyrrole ring contraction. The calculated blue shift of the Q and B bands of **6-2H** relative to **1-2H** (ΔQ1 = −16 nm, ΔQ2 = −1 nm; ΔB1 = −23 nm) closely follows the experimentally observed changes in the absorption spectrum of **1-2H** upon photolysis at 80 K (ΔQ1 = −17 nm, ΔQ2 = −5 nm; ΔB1 = −12 nm), strongly suggesting the observed electronic absorption spectrum of the photointermediate is indeed that of **6-2H**.

The calculated electronic absorption spectra of the internal phenyl insertion photoproduct, **5-2H**, and the initial intermediate formed during its formation, **8-2H**, both show perturbations

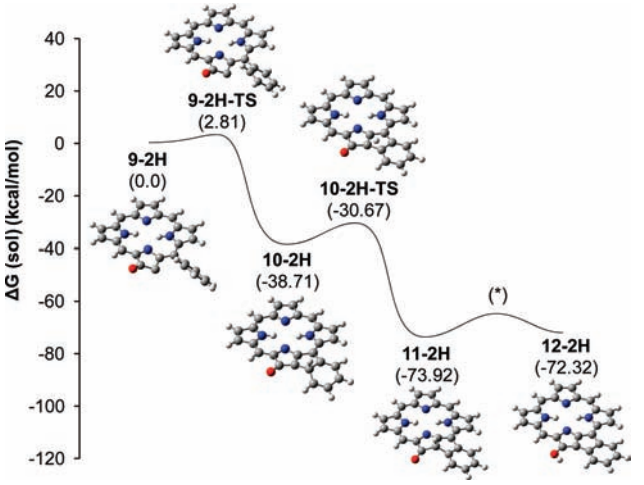

Figure 7. Reaction profile for the progression of the in-plane singlet carbene intermediate (**9-2H**) via the intramolecular insertion of the phenyl C−H bond into the out-of-plane, empty p_z orbital to form **12-2H**. (*This transition state was not found and is shown for illustration only.)

to Gouterman orbitals from the mixing of the phenyl and macrocyclic aromatic systems. The calculated electronic absorptions of **5-2H** consist of Q-bands at 667 and 611 nm and absorptions contributing to the Soret band at 480 and 425 nm. An additional intense electronic excitation from a π orbital primarily based on the inserted phenyl group, HOMO−2, to LUMO+1 (Figure S2c) is predicted at 421 nm and should contribute to the intensity of the Soret band, although the primary electronic transition does not occur between Gouterman orbitals and it is not formally assigned as a Soret peak. No electronic absorption spectrum has been reported for **5-2H**, although the spectra for **5-Cu** and **5-Ni** exhibit red-shifted Q-bands (**5-Ni** = 617 nm, 680 nm; **5-Cu** = 633 nm, 662 nm) versus **1-Cu** and **1-Ni** and broad Soret bands with distinct shoulders (**5-Ni** = 430 nm, 562 nm; **5-Cu** = 430 nm, 447 nm). This is in good agreement with the prediction of a split Soret band and red-shifted Q-bands of **5-2H** versus **2-2H**.

The calculated spectrum of the **8-2H** intermediate is heavily influenced by a relatively low energy LUMO (Figure S2e) arising from the mixing of the exocyclic phenyl and a orbitals. The LUMO+1 and LUMO+2 orbitals exhibit similar aromatic mixing between the exocyclic phenyl group and the other Gouterman π^* orbital and are close in energy (Δ = 0.07 eV). Because they have similar orbital parentages, they are treated as nondegenerate contributors to the same Gouterman orbital for the purposes of assigning visible absorption bands. This Gouterman set is significantly higher in energy than the LUMO Gouterman orbital (0.74 eV), resulting in a large energetic gap between the calculated absorptions at 952 and 637 nm. Although the 315 nm gap between these excitations is much larger than typically observed for porphyrin Q-bands, both of these transitions are between orbitals with macrocyclic electronic distributions consistent with those in the Gouterman model and have thus been assigned as Q-bands. A 599 nm excitation is predicted from the HOMO−2 π orbital to the LUMO and is assigned as $\pi \rightarrow \pi^*$. The remaining visible excitations at 548, 525, and 420 nm all have been assigned as Soret absorptions.

The calculated electronic absorption spectra for **5-2H** and **8-2H** both predict red-shifted Q-bands versus **1-2H**, which is inconsistent with the spectrum observed for the 80 K photointermediate, strongly suggesting that no intramolecular phenyl insertion has occurred in the trapped species.

Phenyl Insertion and Wolff Rearrangement Mechanisms. To help understand the potential photochemical reaction mechanisms of the diazo chlorins, the reactivity of ketocarbene intermediate was computationally investigated. The reaction profile of the internal addition of a phenyl C−H bond was calculated (Figure 7) using a simplified model of **2-2H**, which omitted extraneous phenyl groups to minimize computational time.

The calculated singlet carbene, **9-2H**, has an overall nonplanar geometry, with the carbene-containing pyrrole exhibiting a dihedral twist that orients the carbonyl oxygen slightly above the macrocycle plane and the carbene carbon slightly below. This nonplanar macrocycle geometry agrees well with that predicted for the calculated structure of the tetraphenylated **2-2H** carbene (*vide supra*). Furthermore, this is consistent with computational studies of acyclic singlet keto-carbenes that predict a preferred geometry in which the carbene−carbonyl dihedral angle is orthogonal and orients the carbene orbital in conjugation with the carbonyl π system.[59] The observed distortion from planarity of the carbene pyrrole in **9-2H** is proposed to stem from the system attempting to achieve this lowest-energy orbital orientation, although the geometric constraints of the cyclic carbene inhibit this configuration. Indeed, the carbene electron density is primarily localized in the sp^2 hybridized carbon orbital, canted below the macrocycle plane. The canting of this orbital does result in some mixing of the carbene into the macrocycle π system, although this contribution is not pronounced (Figure S7a). Orthogonal to the sp^2 HOMO is the nonhybridized, carbene p_z LUMO (Figure S7b) that is responsible for the electrophilic character of the carbene. The lowest-energy orientation of the phenyl group is predicted to be twisted toward the carbene, and a weak interaction of the phenyl π electron density with this empty p_z carbene orbital is proposed to account for the stabilization of this geometry.

Consistent with Hammond's postulate, the transition state calculated for the initial phenyl C−H bond insertion, **9-2H-TS**, occurs early on the reaction coordinate and closely resembles **9-2H**. The primary geometric rearrangements are a shortening of the distance between the carbene carbon and the phenyl group and an increase in the twisting of the carbonyl group relative to the carbene lone-pair. The low computational activation energy of 2.8 kcal/mol suggests that rearrangement to this transition state should be facile barring any external geometric inhibition.

The formation of a new bond between the carbene carbon and an *ortho* phenyl carbon results in the optimized **10-2H** structure, which is proposed to be the initial photointermediate formed upon nucleophilic addition to the unoccupied carbene p_z orbital. The intermediate **10-2H** suggests that the C_{ph}−H bond is preserved upon formation of the new C−C bond. Additional starting geometries that bias the system toward a direct C_{ph}−H bond insertion that could result in the concerted migration of the phenyl hydrogen to the carbene carbon were attempted, although these efforts invariably resulted in energy minimizations to **10-2H**. As a result of this C_{ph}−H bond retention, the optimized structure exhibits an sp^3 hybridized phenyl carbon, resulting in the loss of aromaticity of the phenyl group. Thus, it is apparent that a shift of electron density from the phenyl π system to the electron deficient carbene is responsible for the new C−C bond formation. Additionally, the calculated energy of **10-2H** is −41.5 kcal/mol relative to **9-2H-TS** (−38.7 kcal/mol relative to **9-2H**), indicating that this C−C bond formation is highly

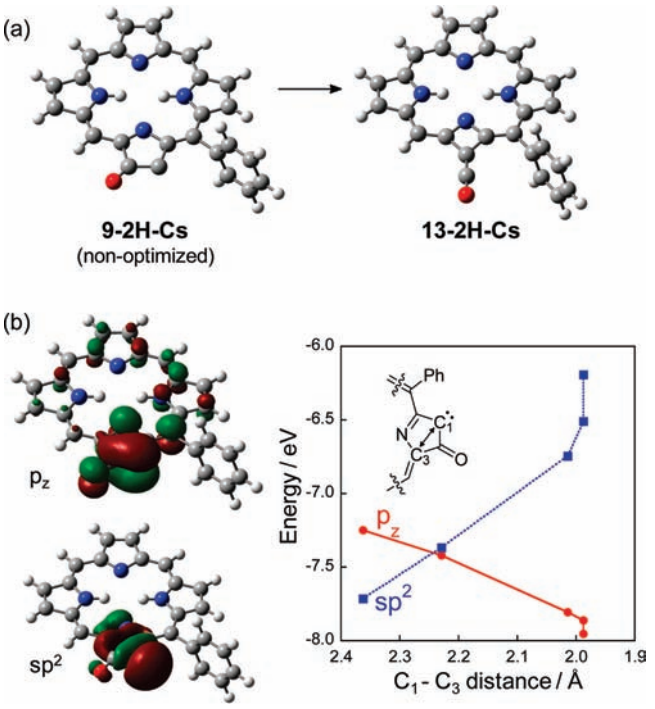

Figure 8. Geometry optimization of **9-2H-Cs** while maintaining C_s symmetry results in a barrierless, *in silico* Wolff rearrangement to form **13-2H-Cs** (a). During this process, the energetic ordering of the p_z and sp^2 orbitals is reversed as the C_1-C_3 distance is decreased (b), forming the "out-of-plane" carbene necessary for the Wolff rearrangement.

energetically favored and is not readily reversible. Reestablishment of phenyl aromaticity is accomplished by migration of the phenyl hydrogen through **10-2H-TS** (−30.7 kcal/mol relative to **9-2H**) to **11-2H** (−73.9 kcal/mol relative to **9-2H**), which is again highly energetically favorable. The final keto−enol tautomerization between **11-2H** and **12-2H** results in a model of the isolated reaction product **5-2H**.

A similar study of the Wolff rearrangement mechanism was performed, although all attempts to effect ketene formation from **9-2H** resulted in insertion of the phenyl C−H bond to form **10-2H**. Close analysis of these attempts showed that the out-of-plane rotation of the carbene carbon during the attempts to form the ketene produced geometries that were very close to that of **9-2H-TS**, and spontaneous phenyl insertion was invariably observed.

It has been proposed[50] that occupancy of the in-plane sp^2 HOMO precludes the Wolff rearrangement because electron density in this orbital creates repulsion between the carbene and the C−C bond, which must insert into the carbene carbon. To facilitate the in-plane Wolff rearrangement and ring contraction, the carbene electron density must be out of the macrocycle plane, and the sp^2 carbene orbital must be partially or fully unoccupied.

Direct attempts at calculating the out-of-plane carbene via energetic reordering of the HOMO and LUMO and accompanying occupancy of the p_z rather than sp^2 orbital of **9-2H** failed to maintain the desired orbital occupation, and instead reoptimized to **9-2H**. This is not surprising because the two orbitals can mix with each other within the C_1 symmetry of the molecule. As an alternate route for calculating the desired electronic configuration, the geometry of the parent diazo-oxochlorin was then optimized with imposed C_s symmetry. This can be easily accomplished by keeping the phenyl group in a perpendicular orientation with respect to the plane of the porphyrin framework. Subsequent *in silico* removal of the diazo group directly affords **9-2H-Cs**. Because the phenyl group plays only a spectator role in the Wolff rearrangement, this is expected to be a minor factor. However, because the sp^2 orbital (a′) and the p_z orbital (a″) have different symmetries in the C_s point group, the electronic state with the desired p_z occupation can be obtained readily. A barrierless Wolff rearrangement to **13-2H-Cs** (Figure 8a) is observed from this orbital occupation, a rearrangement that had not been observed from the **9-2H** starting configuration. Certainly the imposition of C_s symmetry on this optimization precludes spontaneous intramolecular phenyl insertion, but this restriction on rotation of the phenyl group cannot fully account for the spontaneous Wolff rearrangement without observation of a stable carbene intermediate.

A careful analysis of the "Woodward−Hoffmann"-type orbital symmetry conservation principles, in fact, suggests that the out-of-plane carbene should be formed readily during loss of N_2. In more detail, the diazo-region of the initial diazochlorin has two occupied π-orbitals with respect to the porphyrin plane (b_1 symmetry within C_{2v} or a″ symmetry within C_s). If the orbital symmetry is maintained during dissociation, this yields the out-of-plane carbene plus N_2 (each containing one occupied out-of-plane π orbital). Hence, the dissociation of N_2 at low temperature conditions automatically leads to the formation of the "out of plane" carbene. This energetic out-of-plane carbene configuration (Figure 8b) immediately leads to the Wolff rearrangement product without an activation barrier. To understand this, we plot the in-plane and out-of-plane carbene orbital energies of **9-2H-Cs** during this rearrangement. Inspection of the carbene orbital energies shows that while the out-of-plane carbene is the higher energy orbital at the starting point, as the C_1-C_3 distance decreases along the Wolff rearrangement trajectory, an increase in the energy of the sp^2 orbital and an accompanying decrease in the p_z orbital results in the energetic reordering of the two orbitals. Therefore, under the experimental conditions of a frozen matrix and very low temperatures, the facile accessibility of this electronic configuration from a rigidly planar carbene structure suggests that the geometric constraint imposed by the frozen matrix may predispose the diazochlorins toward a barrierless ketene rearrangement rather than the formation of a stable carbene intermediate. It is important to note here that the out-of-plane carbene is not formed by a two-electron excitation process from the in-plane carbene but is directly generated during N_2 dissociation from the diazochlorin in the first place. It then rearranges without any activation barrier to yield the ketene intermediate, as observed.

At higher temperatures, however, it is likely that a significant part of (or most of) the out-of-plane carbene will be converted to the more stable in-plane ground-state carbene, and thus a mixture of out-of-plane and in-plane singlet carbenes is expected. These results are consistent with the formation of the observed products and the computed barriers. In additional support to our observations, by calculating the potential energy surfaces describing these rearrangement pathways for several simple α-diazocarbonyl compounds, Platz has previously shown that subtle geometric changes in the nitrogen-dissociation transition state can induce concerted formation of a ketene in a system that would normally favor progression through a carbene intermediate.[59]

An alternate mechanism for ketene formation from a "vibrationally hot" singlet carbene with sufficient energy to overcome the modest barrier necessary for ketene rearrangement has also been invoked to facilitate high-yield Wolff rearrangements.[56,58,66]

This "hot carbene" has been shown to use residual vibrational energy from the diazo photodissociation reaction to effect spontaneous Wolff rearrangement. The low energetic barrier calculated for the internal insertion of phenyl C−H bond into **9-2H**, coupled with the computational absence of the ketene rearrangement of **9-2H** without phenyl insertion, suggests that any rearrangement of a singlet carbene within our system should preferentially generate an internally quenched product over a ketene. Although the frozen matrix would hinder the rotation of adjacent phenyl groups into the correct orientation for internal C−H bond insertion, the abundance of toluene and BuOH in the matrix would certainly provide ample substrates in close proximity of a carbene to afford carbene addition products, despite the inability of these materials to diffuse within the frozen glass. The absence of detectable amount of **5-M** or any other radical products in any low-temperature photolysis experiments suggests this "hot carbene" pathway does not play a significant role in ketene formation within our system.

CONCLUSIONS

Photolysis of diazochlorins within a frozen matrix has been shown via electronic absorption spectroscopy to generate a single photointermediate that has been identified as a ketene via vibrational spectroscopy. Computational modeling of the IR absorption, Raman, and electronic spectra of potential intermediates supports these assignments. Analysis of the photoproducts generated within the frozen matrix shows near-exclusive formation of ring-contracted azeteo-chlorin photoproducts, suggesting that the thermodynamically favored intramolecular reaction mechanism is the Wolff rearrangement.

Computational investigations of the carbene stability and subsequent reaction trajectory suggest rearrangement of this intermediate to form a ketene species does not readily occur. Instead, imposition of a planar conformation upon the diazochlorins geometrically and electronically biases the system toward direct ketene formation, suggesting that a barrierless Wolff rearrangement during photodissociation of N_2 is responsible for formation of the observed ketene intermediate. The absence of any isolated photoproducts thought to originate from a carbene intermediate further suggests that a "hot carbene" species is not present in the frozen matrix, and therefore does not contribute to ketene formation at low temperature. Therefore, it is clear that this ketene intermediate is not responsible for the diversity of photoproducts observed upon solution photolysis of diazochlorins because reactions performed within frozen matrices selectively and exclusively generate azeteoporphyrins. The overarching implication is that azeteoporphyrin formation via the Wolff rearrangement is very sensitive to the structural disposition and dynamics of the adjacent framework, and specific reaction intermediate formation can be influenced markedly by this chemical parameter.

ASSOCIATED CONTENT

Supporting Information. Experimental details as well as low temperature photolysis data and electronic structure calculation results. This material is available free of charge via the Internet at http://pubs.acs.org.

AUTHOR INFORMATION

Corresponding Author
zaleski@indiana.edu

ACKNOWLEDGMENT

The support of Indiana University is gratefully acknowledged. We would like to thank Professor Daniel J. Mindiola for the use of the Specac low temperature IR accessory.

REFERENCES

(1) Dougherty, T. J.; Gomer, C. J.; Henderson, B. W.; Jori, G.; Kessel, D.; Korbelik, M.; Moan, J.; Peng, Q. *J. Natl. Cancer Inst.* **1998**, *90*, 889.
(2) Hagiya, Y.; Adachi, T.; Ogura, S.-I.; An, R.; Tamura, A.; Nakagawa, H.; Okura, I.; Mochizuki, T.; Ishikawa, T. *J. Exp. Ther. Oncol.* **2008**, *7*, 153.
(3) Josefsen, L. B.; Boyle, R. W. *Met.-Based Drugs* **2008**, *2008*, 276109.
(4) Juarranz, A.; Jaen, P.; Sanz-Rodriguez, F.; Cuevas, J.; Gonzalez, S. *Clin. Transl. Oncol.* **2008**, *10*, 148.
(5) Karotki, A.; Khurana, M.; Lepock, J. R.; Wilson, B. C. *Photochem. Photobiol.* **2006**, *82*, 443.
(6) Silva, J. N.; Filipe, P.; Morliere, P.; Maziere, J.-C.; Freitas, J. P.; Cirne De Castro, J. L.; Santus, R. *Bio-Med. Mater. Eng.* **2006**, *16*, S147.
(7) Szurko, A.; Kraemer-Marek, G.; Widel, M.; Ratuszna, A.; Habdas, J.; Kus, P. *Acta Biochim. Pol.* **2003**, *50*, 1165.
(8) Wu, L.; Yang, L.; Huang, J.; Zhang, L.; Weng, X.; Zhang, X.; Shen, C.; Zhou, X.; Zheng, C. *Chem. Biodiversity* **2009**, *6*, 1066.
(9) Ambroise, A.; Wagner, R. W.; Rao, P. D.; Riggs, J. A.; Hascoat, P.; Diers, J. R.; Seth, J.; Lammi, R. K.; Bocian, D. F.; Holten, D.; Lindsey, J. S. *Chem. Mater.* **2001**, *13*, 1023.
(10) Bernini, R.; Tonezzer, M.; Mottola, F.; Zeni, L.; Quaranta, A.; Maggioni, G.; Carturan, S.; Mea, G. *Sens. Actuators, B* **2007**, *127*, 231.
(11) Cho, Y.-J.; Ahn, T. K.; Song, H.; Kim, K. S.; Lee, C. Y.; Seo, W. S.; Lee, K.; Kim, S. K.; Kim, D.; Park, J. T. *J. Am. Chem. Soc.* **2005**, *127*, 2380.
(12) Di Natale, C.; Salimbeni, D.; Paolesse, R.; Macagnano, A.; D'Amico, A. *Sens. Actuators, B* **2000**, *65*, 220.
(13) He, X.; Liu, H.; Li, Y.; Liu, Y.; Lu, F.; Li, Y.; Zhu, D. *Macromol. Chem. Phys.* **2005**, *206*, 2199.
(14) Jang, J. H.; Jeon, K.-S.; Oh, S.; Kim, H.-J.; Asahi, T.; Masuhara, H.; Yoon, M. *Chem. Mater.* **2007**, *19*, 1984.
(15) Liu, C.-y.; Bard, A. J. *Acc. Chem. Res.* **1999**, *32*, 235.
(16) Liu, C.-y.; Tang, H.; Bard, A. J. *J. Phys. Chem.* **1996**, *100*, 3587.
(17) Sgobba, V.; Giancane, G.; Conoci, S.; Casilli, S.; Ricciardi, G.; Guldi, D. M.; Prato, M.; Valli, L. *J. Am. Chem. Soc.* **2007**, *129*, 3148.
(18) Amao, Y.; Komori, T. *Langmuir* **2003**, *19*, 8872.
(19) Campbell, W. M.; Jolley, K. W.; Wagner, P.; Wagner, K.; Walsh, P. J.; Gordon, K. C.; Schmidt-Mende, L.; Nazeeruddin, M. K.; Wang, Q.; Gratzel, M.; Officer, D. L. *J. Phys. Chem. C* **2007**, *111*, 11760.
(20) Cheng, Y.-J.; Yang, S.-H.; Hsu, C.-S. *Chem. Rev.* **2009**, *109*, 5868.
(21) Cherian, S.; Wamser, C. C. *J. Phys. Chem. B* **2000**, *104*, 3624.
(22) Hasselman, G. M.; Watson, D. F.; Stromberg, J. R.; Bocian, D. F.; Holten, D.; Lindsey, J. S.; Meyer, G. J. *J. Phys. Chem. B* **2006**, *110*, 25430.
(23) Jasieniak, J.; Johnston, M.; Waclawik, E. R. *J. Phys. Chem. B* **2004**, *108*, 12962.
(24) Kay, A.; Graetzel, M. *J. Phys. Chem.* **1993**, *97*, 6272.
(25) Kim, H.-S.; Kim, C.-H.; Ha, C.-S.; Lee, J.-K. *Synth. Met.* **2001**, *117*, 289.
(26) Nocera, D. G. *Inorg. Chem.* **2009**, *48*, 10001.
(27) Takahashi, K.; Takano, Y.; Yamaguchi, T.; Nakamura, J.-i.; Yokoe, C.; Murata, K. *Synth. Met.* **2005**, *155*, 51.
(28) Hasobe, T.; Fukuzumi, S.; Kamat, P. V. *J. Phys. Chem. B* **2006**, *110*, 25477.
(29) Huang, X.; Zhu, C.; Zhang, S.; Li, W.; Guo, Y.; Zhan, X.; Liu, Y.; Bo, Z. *Macromolecules* **2008**, *41*, 6895.
(30) Imahori, H.; Kang, S.; Hayashi, H.; Haruta, M.; Kurata, H.; Isoda, S.; Canton, S. E.; Infahsaeng, Y.; Kathiravan, A.; Pascher, T. R.; Chábera, P.; Yartsev, A. P.; Sundström, V. *J. Phys. Chem. A* **2011**, *115*, 3679.

(31) Kira, A.; Umeyama, T.; Matano, Y.; Yoshida, K.; Isoda, S.; Park, J. K.; Kim, D.; Imahori, H. *J. Am. Chem. Soc.* **2009**, *131*, 3198.
(32) Kongkanand, A.; Domínguez, R. M.; Kamat, P. V. *Nano Lett.* **2007**, *7*, 676.
(33) Lin, Y.-Y.; Chu, T.-H.; Li, S.-S.; Chuang, C.-H.; Chang, C.-H.; Su, W.-F.; Chang, C.-P.; Chu, M.-W.; Chen, C.-W. *J. Am. Chem. Soc.* **2009**, *131*, 3644.
(34) Loi, M. A.; Denk, P.; Hoppe, H.; Neugebauer, H.; Winder, C.; Meissner, D.; Brabec, C.; Sariciftci, N. S.; Gouloumis, A.; Vázquez, P.; Torres, T. *J. Mater. Chem.* **2003**, *13*, 700.
(35) Said, A. J.; Poize, G.; Martini, C.; Ferry, D.; Marine, W.; Giorgio, S.; Fages, F.; Hocq, J.; Bouclé, J.; Nelson, J.; Durrant, J. R.; Ackermann, J. *J. Phys. Chem. C* **2010**, *114*, 11273.
(36) Takahashi, K.; Iwanaga, T.; Yamaguchi, T.; Tomura, T.; Murata, K. *Synth. Met.* **2001**, *123*, 91.
(37) Takechi, K.; Shiga, T.; Akiyama, T.; Yamada, S. *Appl. Phys. Express* **2010**, *3*, 122301.
(38) Chandra, T.; Kraft, B. J.; Huffman, J. C.; Zaleski, J. M. *Inorg. Chem.* **2003**, *42*, 5158.
(39) Nath, M.; Huffman, J. C.; Zaleski, J. M. *J. Am. Chem. Soc.* **2003**, *125*, 11484.
(40) Nath, M.; Huffman, J. C.; Zaleski, J. M. *J. Chem. Soc., Chem. Commun.* **2003**, 858.
(41) Nath, M.; Pink, M.; Zaleski, J. M. *J. Am. Chem. Soc.* **2005**, *127*, 478.
(42) Spence, J. D.; Cline, E. D.; LLagostera, D. M.; O'Toole, P. S. *J. Chem. Soc., Chem. Commun.* **2004**, 180.
(43) Spence, J. D.; Hargrove, A. E.; Crampton, H. L.; Thomas, D. W. *Tetrahedron Lett.* **2007**, *48*, 725.
(44) Fouad, F. S.; Crasto, C. F.; Lin, Y.; Jones, G. B. *Tetrahedron Lett.* **2004**, *45*, 7753.
(45) Aihara, H.; Jaquinod, L.; Nurco, D. J.; Smith, K. M. *Angew. Chem., Int. Ed.* **2001**, *40*, 3439.
(46) Köpke, T.; Pink, M.; Zaleski, J. *Synlett* **2006**, *2006*, 2183.
(47) Köpke, T.; Pink, M.; Zaleski, J. *Synlett* **2008**, *2008*, 1882.
(48) Köpke, T.; Pink, M.; Zaleski, J. M. *J. Chem. Soc., Chem. Commun.* **2006**, *1*, 4940.
(49) Köpke, T.; Pink, M.; Zaleski, J. M. *Org. Biomol. Chem.* **2006**, *4*, 4059.
(50) Köpke, T.; Pink, M.; Zaleski, J. M. *J. Am. Chem. Soc.* **2008**, *130*, 15864.
(51) Kirmse, W. *Eur. J. Org. Chem.* **2002**, *2002*, 2193.
(52) McMahon, R. J.; Chapman, O. L.; Hayes, R. A.; Hess, T. C.; Krimmer, H. P. *J. Am. Chem. Soc.* **1985**, *107*, 7597.
(53) Wang, J.-L.; Toscano, J. P.; Platz, M. S.; Nikolaev, V.; Popik, V. *J. Am. Chem. Soc.* **1995**, *117*, 5477.
(54) Toscano, J. P.; Platz, M. S.; Nikolaev, V.; Popic, V. *J. Am. Chem. Soc.* **1994**, *116*, 8146.
(55) Burdzinski, G. T.; Wang, J.; Gustafson, T. L.; Platz, M. S. *J. Am. Chem. Soc.* **2008**, *130*, 3746.
(56) Burdzinski, G.; Réhault, J.; Wang, J.; Platz, M. S. *J. Phys. Chem. A* **2008**, *112*, 10108.
(57) Wang, J.; Burdzinski, G.; Kubicki, J.; Gustafson, T. L.; Platz, M. S. *J. Am. Chem. Soc.* **2008**, *130*, 5418.
(58) Burdzinski, G.; Platz, M. S. *J. Phys. Org. Chem.* **2010**, *23*, 308.
(59) Popik, V. V. *Can. J. Chem.* **2005**, *83*, 1382.
(60) Foresman, J. B.; Frisch, E. *Exploring Chemistry With Electronic Structure Methods*; Gaussian, Inc.: Pittsburgh, PA, 1996.
(61) Gouterman, M. *J. Mol. Spectrosc.* **1961**, *6*, 138.
(62) Gouterman, M.; Wagniere, G.; Snyder, L. *J. Mol. Spectrosc.* **1963**, *11*, 108.
(63) Baerends, E. *Coord. Chem. Rev.* **2002**, *230*, 5.
(64) Chen, D.-M.; Liu, X.; He, T.-J.; Liu, F.-C. *Chem. Phys.* **2003**, *289*, 397.
(65) Venkataramanan, N. S.; Suvitha, A.; Nejo, H.; Mizuseki, H.; Kawazoe, Y. *Int. J. Quantum Chem.* **2011**, *111*, 2340.
(66) Burdzinski, G. T.; Middleton, C. T.; Gustafson, T. L.; Platz, M. S. *J. Am. Chem. Soc.* **2006**, *128*, 14804.